Materials Science & Engineering A 830 (2022) 142313

Contents lists available at ScienceDirect

Materials Science & Engineering A

journal homepage: www.elsevier.com/locate/msea

Extraordinary fracture toughness in nickel induced by heterogeneous grain structure

Shengde Zhang [a,b,1], Muxin Yang [a,1], Fuping Yuan [a,b,*], Lingling Zhou [a,b], Xiaolei Wu [a,b]

[a] State Key Laboratory of Nonlinear Mechanics, Institute of Mechanics, Chinese Academy of Science, 15 Beisihuan West Road, Beijing, 100190, China
[b] School of Engineering Science, University of Chinese Academy of Sciences, 19A Yuquan Road, Beijing, 100049, China

ARTICLE INFO

Keywords:
Heterogeneous grain structures
Fracture toughness
J-R curves
Ductility
Strain hardening

ABSTRACT

The tensile properties and fracture toughness of both heterogeneous grain structures and homogeneous structures in pure nickel have been investigated and compared. The heterogeneous samples were found to show much larger uniform elongation and much higher fracture toughness at the similar level of yield strength, compared to the homogeneous structures. The enhanced ductility/toughness can be attributed to the stronger hetero-deformation-induced hardening for the heterogeneous structures. In sharp contrast to the cleavage-like and brittle fracture behavior in the homogeneous hot-extruded and cold-rolled samples, the fracture process in the heterogeneous structures shows ductile fracture by microvoid coalescence and dimples. The crack path in the heterogeneous structures was found to display a gourd shape, which can result in longer crack length and dissipate more energy for better fracture toughness. Hardening is obvious across a much larger area around the crack tip in the heterogeneous structures as compared to the homogeneous structures, indicating a much larger plastic zone for the heterogeneous structures. The strong strain hardening at the crack tip was found to be induced by the grain refinement of the coarse grains in the heterogeneous structures, resulting in extraordinary fracture toughness.

1. Introduction

Applications of coarse grained (CG) metals are limited by their low yield strength, and such limitation can be resolved by introducing various kinds of defects, such as grain boundaries (GBs), twin boundaries (TBs) or high density of dislocations [1–3]. Simple cold working or grain refinement into nanoscale by severe plastic deformation (SPD) can achieve high strength in metals, while the strain hardening capacity and the tensile ductility are scarified significantly at the same time [4–8]. Recently, a strategy employing strain gradients and geometrically necessary dislocations (GNDs) has been proposed to obtain high strength and large ductility [9–20]. This strategy is aiming to design heterogeneous structures containing various domains with dramatically different mechanical properties, thus stress/strain partitioning and hetero-deformation-induced (HDI) strengthening/hardening have been found to play crucial roles in their strain hardening behaviors [12–19, 21].

Damage tolerance and fracture toughness are also important mechanical parameters for engineering structural applications [22–41], besides the strength and ductility. Usually, the fracture toughness of metals is dependent on the ability of their microstructures to absorb the deformation energy for crack initiation and propagation. Both high strength and high fracture toughness are desired in most structural applications, while unfortunately these two properties are mutually exclusive in general [22]. It has been reported that the fracture toughness can be improved in materials in two ways: intrinsic and extrinsic toughening mechanisms [22]. Intrinsic toughening mechanism is primarily associated with the strain hardening capacity and the plasticity of materials, which is effective against both the initiation and propagation of cracks by enlarging the plastic zone. While, extrinsic toughening mechanism is related to processes, such as crack bridging, for reducing (shielding) the concentration of the local stresses and strains ahead the crack tip.

Intrinsic toughening mechanism is the primary source of fracture resistance for most metals and alloys, thus the conflict between strength and fracture toughness still exists for metals and alloys with

* Corresponding author. State Key Laboratory of Nonlinear Mechanics, Institute of Mechanics, Chinese Academy of Science, 15 Beisihuan West Road, Beijing, 100190, China.
E-mail address: fpyuan@lnm.imech.ac.cn (F. Yuan).
[1] These two authors contributed equally to this work.

https://doi.org/10.1016/j.msea.2021.142313
Received 27 August 2021; Received in revised form 5 November 2021; Accepted 7 November 2021
Available online 9 November 2021

homogeneous microstructures [22,23]. Heterogeneous structures have displayed high strength, strong strain hardening capacity and large ductility under tensile loading [9–20], which provides them as ideal candidates for overcoming the strength-toughness dilemma [23–28]. It is well known that extra hardening can be achieved in heterogeneous structures due to the GNDs induced by the deformation incompatibility between varying domains with significant difference in mechanical properties [13,15,17,21], and the resultant strong strain hardening capacity should have beneficial effects on their fracture behaviors. While, how the enhanced strain hardening behaviors of heterogeneous structures affect the initiation and propagation of cracks is still an open question. Moreover, the relationship between the crack propagation path and the hard/soft domains need be clarified. In this perspective, a heterogeneous grain structure was architected in pure nickel by SPD and subsequent critical annealing (partially recrystallized), and then the tensile and fracture behaviors of Ni with heterogeneous grain structure were systematically investigated. Only dislocation behaviors involve during quasi-static plastic deformation in pure Ni, thus we can consider the pure Ni as a model material for focusing on the effects of heterogeneous grain structures only on the fracture behaviors, and the other issues, such as deformation twins and phase transformation, can be excluded.

2. Materials and experimental procedures

The received hot-extruded (HE) rods (extrusions from Ø25 to Ø16 mm at a relatively low temperature of 723 K) have a diameter of 16 mm, and the chemical composition for the commercial pure nickel is 99.9Ni-others (in mass %). The received HE rods were first annealed at 973 K for 2 h to obtain a homogeneous CG structure. The thickness for the fracture tests should be large enough according to the ASTM standard E1820. Thus, a combination of ECAP with A route and CR was used for severe plastic deformation, and the A route was chosen because the deformation in ECAP (two passes) with A route is very similar to that in CR process [42]. The annealed rods were processed by equal channel angular pressing (ECAP) using a split die with two channels intersecting at an inner angle of 90° and an outer angle of 35°. The rods for ECAP have dimensions of Ø16 mm × 90 mm. The bars were processed for 2 passes (2P) at room temperature using route A, yielding an effective strain about 1 by each pass. After ECAP, the deformed billets were machined into plates with a thickness of about 12 mm, and the plates were cold-rolled (CR) with a thickness reduction of 41.6%. The CR plates have a final thickness of about 7 mm. The procedure for processing materials is shown in Fig. 1a. In order to obtain various heterogeneous microstructures, the CR plates were annealed at varying temperatures in the range of 673–973 K for 2 h, followed by cooling in air. These annealing temperatures were selected based on the hardness evolution curve as a function of annealing temperature from the previous study [43], in which the temperature range for the transition stage from the high hardness plateau to the low hardness plateau is between 700 and 780 K. Thus, the samples annealed at 698, 723, 748, 773 K can be considered as partial recrystallized samples with heterogeneous structures and named as HS1, HS2, HS3 and HS4, respectively. While, the samples annealed at 798 and 973 K can be considered as fully recrystallized samples with homogeneous CG structures and named as CG1 and CG2, respectively.

The plate specimens for quasi-static tensile testing have a dog-bone shape, and the dimensions of gauge section are 10 × 2.5 × 1 mm^3. The quasi-static uniaxial tensile tests and load-unload-reload (LUR) tests were conducted using an MTS landmark testing machine at a strain rate of 5 × 10^{-4}/s and at room temperature under displacement control. Three tensile tests were conducted for each specimen to check the repeatability for experimental data. The tensile direction was set to be parallel to the rolling direction. During LUR tests, the specimens were first elongated to a designated strain, then the specimens were unloaded by the stress-control mode to 20 N at the unloading rate of 200 N/min, followed by reloading. An extensometer was used to accurately measure and control the displacement during the tensile tests and LUR tests.

For the fracture toughness tests, miniaturized compact tension (CT) specimens were cut from the hot-rolled bars, the CR and annealed plates with the crack direction perpendicular to the rolling direction. The configuration for cutting the specimens from the plates is displayed in Fig. 1b. The fracture specimens have a width, W, of 12 mm, a thickness, B, of 6 mm, and an initial notch depth, a_0 of about 5.4 mm. The fracture

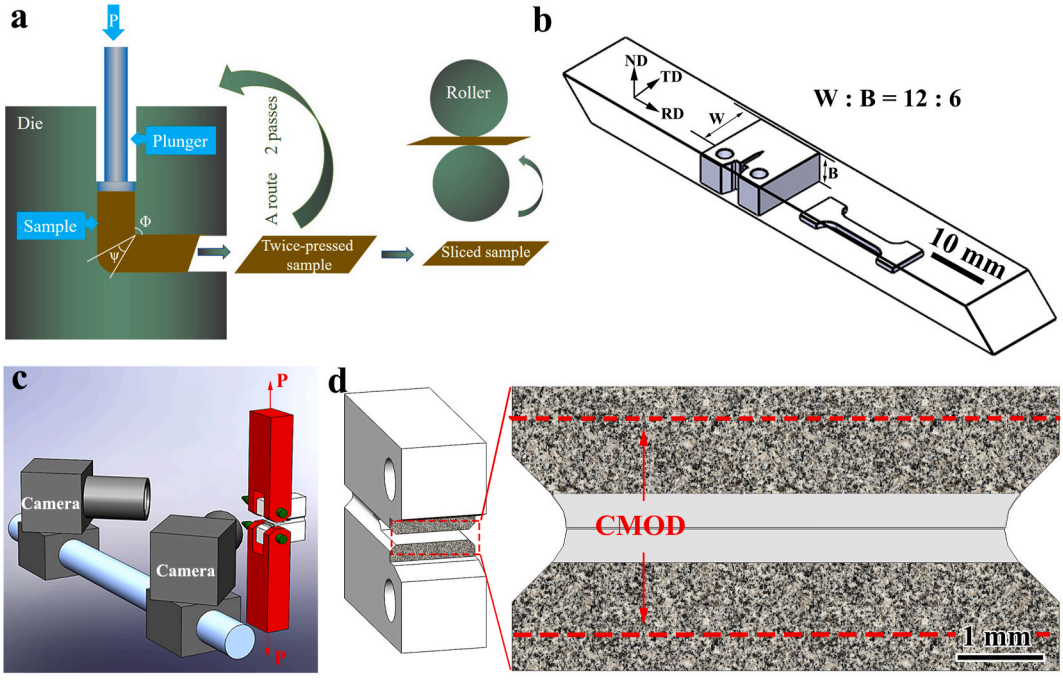

Fig. 1. (a) The procedure for processing materials. (b) The configuration for cutting the specimens from the plates. (c) (d) The configuration of fracture toughness test with a contactless VCOD gauging system.

specimens were further pre-cracked by fatigue under tension-tension loading to produce a sharp crack tip until a total crack length of about 6.0 mm (~ 0.5 W). In order to avoid pronounced crack tunneling and invalid data for obtaining fracture toughness as cracks propagate in planar specimens, side grooves at both surfaces with a total depth of 0.2*B* were intentionally machined to enhance the surface stress constraint and make cracks extend straightly. The fracture tests were conducted by an MTS landmark machine with cross-head speed of 0.3 mm/min under displacement control. The load-line displacement curves for fracture tests were determined by measuring the crack mouse opening displacements (CMOD) using a contactless video crack opening displacement (VCOD) gauging system (as shown in Fig. 1c and d). In the VCOD gauging system, the initial high-contrast stochastic spot patterns were created on the sample surface of the fracture specimens, a commercial software ARAMIS was applied to analyze the digital image correlation (DIC) data and the used facet size for the CMOD calculation was 50 μm. Then the instantaneous crack length was determined using the unloading compliance technique [28] and the data from the VCOD gauging system. The elastic-plastic *J*-integral fracture resistance curves as a function of crack extension (*J*-*R* curves) were obtained using the procedure recommended in the ASTM standard E1820. For each sample, three fracture tests were conducted and the error bars for the fracture toughness were provided.

Scanning electron microscope (SEM) was used to characterize the fracture surface after fracture tests. Electron backscattered diffraction (EBSD) and transmission electron microscope (TEM) techniques have been utilized to reveal the microstructures before and after mechanical testing. The details for sample preparation of EBSD and TEM can be found elsewhere [13,44]. Kernel average misorientation (KAM) was calculated against the first nearest neighbor ignoring the misorientation larger than 3°. The distributions of micro-hardness around the crack tips for various samples after fracture tests were also obtained using a Vickers diamond indenter under a load of 25 g for 15 s dwell time.

3. Results and discussions

3.1. Microstructure characterization before mechanical testing

The microstructures for the typical samples (the CR sample, the two partial recrystallized samples, HS1 and HS2) before the mechanical tests are shown in Fig. 2 by EBSD (inverse pole figure, IPF). In Fig. 2b2 and 2c2, only the distributions of recrystallized CG are displayed by blacking out the ultrafine-grained (UFG) area. The CR sample displays a typical lamellar deformed structure along the rolling direction (Fig. 2a1). While the EBSD image for the other perpendicular plane show a relatively equi-axed deformed structure (Fig. 2a2). The two partial recrystallized samples display heterogeneous structures (named as HS2 and HS1, as shown in Fig. 2b1-2b2 and 2c1-2c2), and the IPF maps in Fig. 2b2 and 2c2 indicate that the area fraction and the average grain size of the recrystallized CG increase with increasing annealing temperature. The area fraction of the recrystallized CG is 45.3% and 5.7% for the HS2 and HS1 samples, respectively. The average grain size of the recrystallized CG is 16.6 and 9.8 μm for the HS2 and HS1 samples, respectively.

The microstructure characterizations for the HE sample by EBSD and TEM are shown in Fig. 3. The HE sample has a slightly elongated grain structure along the extrusion direction (Fig. 3a), while has an equi-axed grain structure with an average grain size of about 50 μm for the plane perpendicular to the extrusion direction (Fig. S1b1). However, high density dislocations are shown in the HE sample, as indicated by the KAM map in Fig. 3b. TEM images for the HE samples showing substructures in the grain interiors are also displayed in Fig. 3c-f. Besides the sharp high-angle GBs, high density of dislocations, dislocation tangles, dislocation walls and dislocations cells at sub-micron level can be observed for the HE sample. These substructures can be considered as low-angle GBs, thus the HE samples can be considered to have UFGs (substructures, low-angle GBs). The UFGs (substructures, low-angle GBs) for the HE samples can be attributed to the severe plastic deformation (from Ø25 to Ø16) at relatively low temperatures (723 K) during the HE process.

TEM images for one typical heterogeneous structure (the HS2 sample

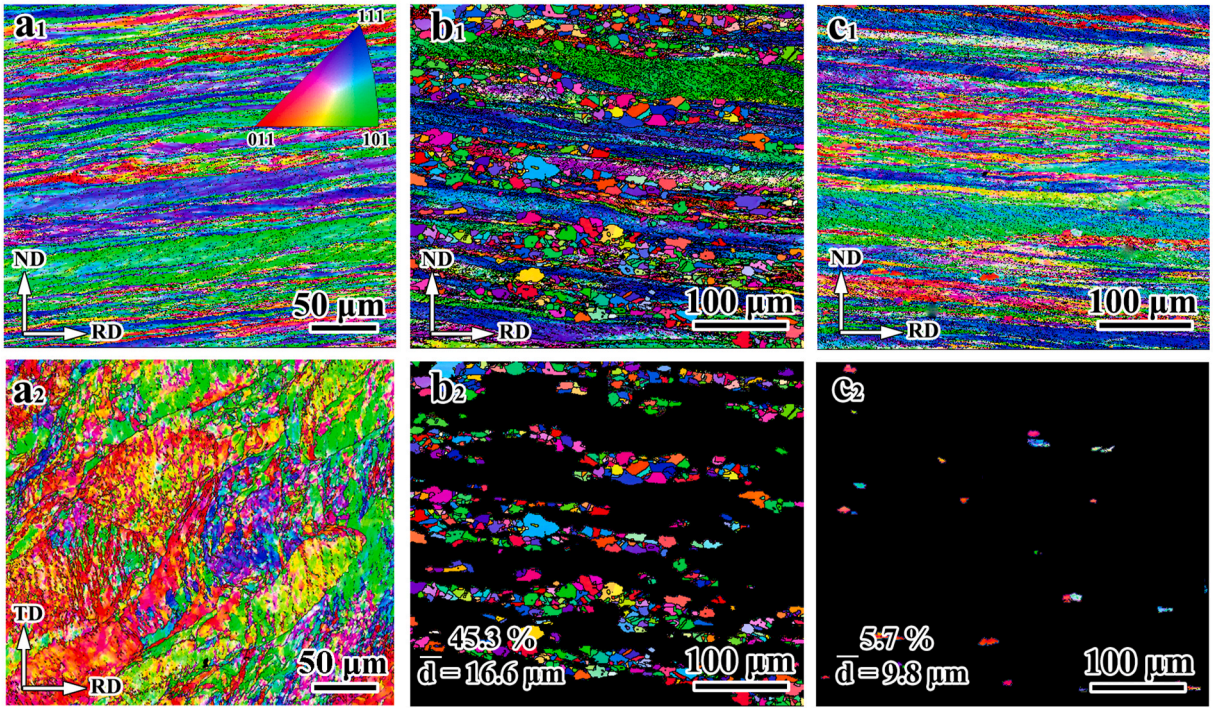

Fig. 2. The IPF images before the mechanical tests for the typical samples: (a1) the CR sample for the TD plane; (a2) the CR sample for the ND plane; (b1) (b2) the HS2 sample; (c1) (c2) the HS1 sample.

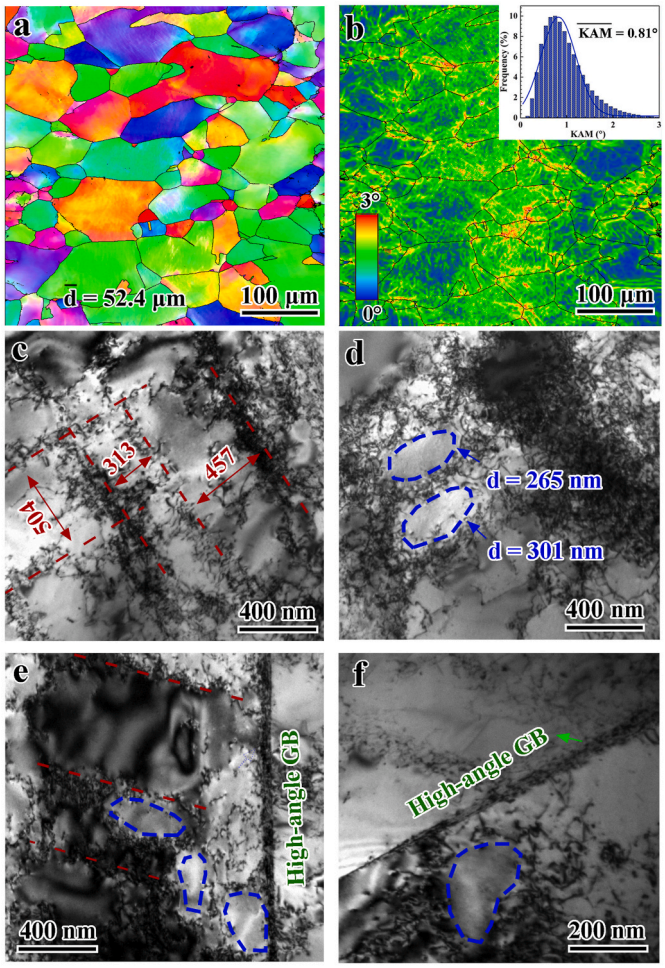

Fig. 3. Microstructure observation for the HE sample before the mechanical tests. (a) The IPF image. (b) The corresponding KAM map. (c)–(f) TEM images.

are shown in Fig. 4. As indicated in Fig. 4a, both the recrystallized CG area and the retained UFG area can be clearly observed for the heterogeneous structure. Sharp GBs can be well identified for the recrystallized CG, and the grain interior is relatively clean in the recrystallized CG, indicating low dislocation density for the recrystallized CG (Fig. 4b). While the retained UFG area displays high density of dislocations and dislocation tangles. The grain size of the recrystallized CG is shown to be about several or tens of μm, which is consistent with the aforementioned EBSD figure.

The EBSD images in two planes (TD and RD) and the corresponding textures for the HE samples are displayed in Fig. S1. Moreover, the EBSD images in two planes (TD and ND) and the corresponding textures for the CR, HS1 and HS2 samples are shown in Figs. S2–S4, respectively. The HE samples show an obvious <100> texture along the extrusion direction, and the grains are slightly elongated along the extrusion direction. The samples after ECAP and CR show a typical rolling-like texture (Fig. S2) as reported in the previous studies [45–47]. The HS1 and HS2 samples also show the typical CR texture, but the texture's strength was reduced during annealing and the retained CR texture becomes weaker with increasing annealing temperature. As shown, the CR, HS1 and HS2 samples have elongated grains for the un-recrystallized area along the rolling direction, but show an equi-axed grain structure observed from the ND direction. Thus, these samples show similar microstructure anisotropy and texture, which should have influences on the mechanical properties. For example, the fracture toughness would be higher due to crack delamination when the crack propagates along some specific direction [48]. While, the tensile tests and the fracture tests have been done along the same directions for all samples, thus the effects of anisotropy and texture should be minimized when considering the effects of homogeneous and heterogeneous grain structures on the mechanical properties.

3.2. Tensile properties and fracture toughness

The tensile properties for various samples are shown in Fig. 5. The engineering stress-strain curves for various samples are displayed in Fig. 5a. The points for yield strength and the ultimate strength are marked by circles and squares, respectively. The yield strength is observed to decrease and the uniform elongation is observed to increase with increasing annealing temperature. It is indicated that the heterogeneous structures have a better synergy of strength and ductility compared to the homogeneous structures. For example, the HS2 sample has a similar yield strength and a much larger uniform elongation, compared to the HE sample. The HS1 sample displays a slightly lower yield strength and a much larger uniform elongation of about 5%, compared to the CR sample (nearly zero uniform elongation, necking right after yielding). As indicated in previous research [12,13,15,17,21,49,50], excellent synergy of strength and ductility can be achieved by heterogeneous structure (such as heterogeneous lamella structures [13],

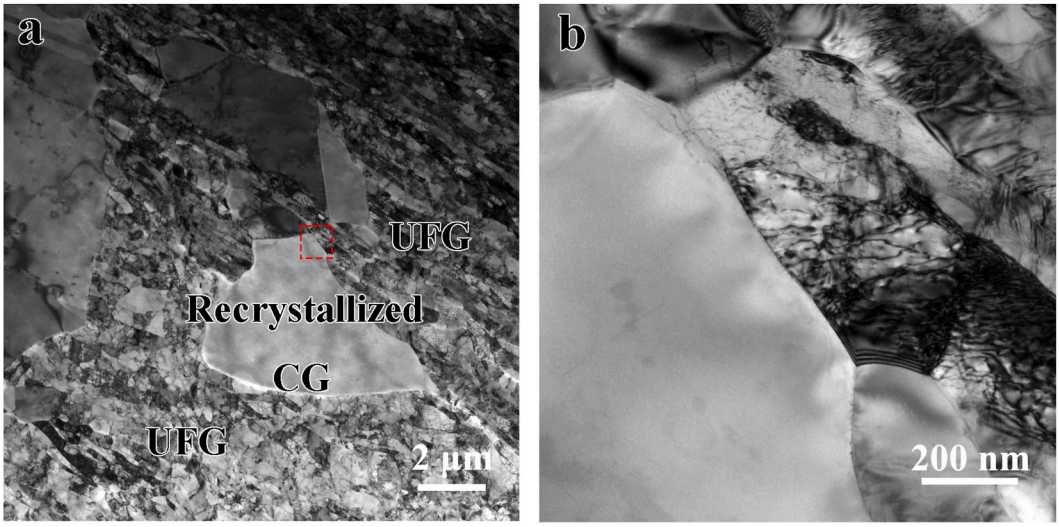

Fig. 4. The TEM bright-field images before the mechanical tests for the HS2 sample.

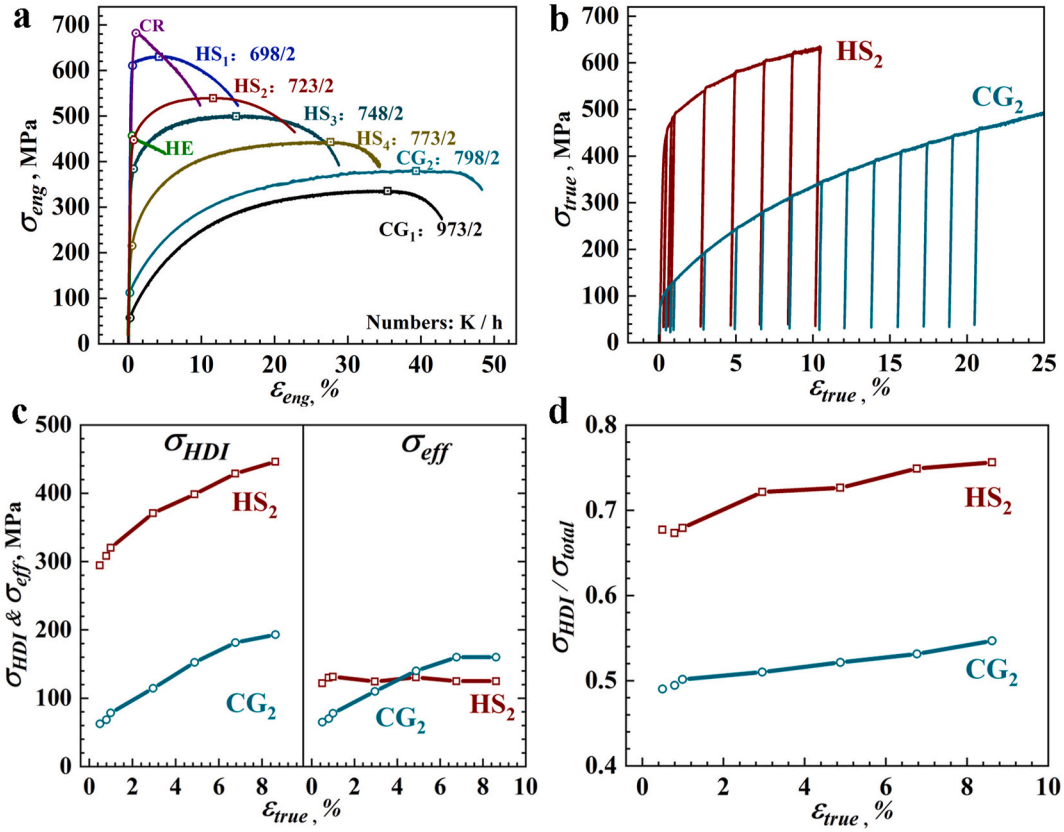

Fig. 5. The quasi-static tensile properties. (a) The engineering stress-strain curves for various samples. (b) The true stress-true strain curves for the LUR tests of the HS2 sample and the CG sample. (c) The evolutions of both back stress and effective stress as a function of applied tensile strain for the HS2 sample and the CG sample. (d) The evolutions of $\sigma_{HDI}/\sigma_{total}$ as a function of applied tensile strain for the HS2 sample and the CG sample.

heterogeneous grain structures [50] and gradient structures [12,49]) due to the HDI hardening, which can be attributed to the back stress that arises from plastic deformation incompatibility between hard and soft domains. In order to illustrate the HDI hardening effect on the tensile properties for the current heterogeneous grain structures, the back stresses for one heterogeneous sample (HS2) and one homogeneous sample (CG) have been measured using LUR tests, as indicated by the true stress-strain curves for LUR tests in Fig. 5b. Using the method proposed in our previous paper [17], the back stress can be calculated by the average value of the unloading yield stress and the reloading yield stress ($\sigma_{HDI} = (\sigma_u + \sigma_r)/2$) from the hysteresis loops of LUR tests. Moreover, the effective stress can be estimated from the total flow stress and the back stress by the following equation: $\sigma_{eff} = \sigma_{total} - \sigma_{HDI}$. Thus, the evolutions of both back stress and effective stress as a function of applied tensile strain for the HS2 sample and the CG sample are displayed in Fig. 5c. In general, $\sigma_{HDI}/\sigma_{total}$ could be considered as the contribution of HDI hardening [21] to the overall strain hardening, thus $\sigma_{HDI}/\sigma_{total}$ is plotted as a function of applied tensile strain for the HS2 sample and the CG sample in Fig. 5d. It is interesting to note that $\sigma_{HDI}/\sigma_{total}$ is larger and increases with a faster rate with increasing applied tensile strain for the HS2 sample, compared to the CG sample. This observation indicates that the HDI hardening should play a much more important role during the tensile deformation for the heterogeneous structures, resulting in better tensile properties.

Four samples have been selected as candidates for fracture toughness tests, i.e., the CR sample and the HS1 sample, the HE sample and the HS2 sample. The HS1 and HS2 samples are heterogeneous structures, while the CR sample and the HE sample are homogeneous structures. The HS1 sample has a slightly lower yield strength and a much higher tensile ductility, as compared to the CR sample, thus those two samples can be considered as a pair for comparison on fracture toughness. Moreover, the HS2 sample has a similar yield strength and a much higher tensile ductility, as compared to the HE sample, thus those two samples can also be considered as a pair for comparison on fracture toughness. Fig. 6a shows the curves of force P as a function of displacement for the four samples. It is obvious that the ratios of maximum force P_{max} to P_Q (which is the point where a line with a slope 95% of the slope of the initial linear part intersects with the curves) are all larger than 1.1, which can be attributed to the substantial crack tip plastic deformation before crack extension. Thus, the direct determination of the critical stress-intensity factor K_{IC} under the linear-elastic plane strain condition is invalid any more. The J-integral method based on the elastic-plastic fracture mechanics was used instead.

The calculated J-integral is plotted as a function of crack extension (Δa) for the four samples in Fig. 6b (J-R curves). Since all samples exhibit stable crack extension, the critical J-integral value J_Q can be taken as the intersection of the J-R curves with 0.2 mm offset blunting lines ($J=2\sigma^*\Delta a$, σ^* where is the average value of the yield strength and the ultimate strength from the quasi-static tensile testing). Both the sample thickness (larger than $10J_Q/\sigma^*$) and the initial crack ligament (b_0=W-a_0) are satisfied with the ASTM standard E1820, and the straight crack extension is guaranteed by the side grooves. Thus J_Q can represent the size-independent intrinsic fracture toughness, and the corresponding critical stress intensity factor K_{IC} can be obtained by the following equation:

$$K_{IC} = \sqrt{\frac{EJ_{IC}}{1-\nu^2}} \quad (1)$$

Where E=200 GPa and ν=0.3 are the Young's modulus and the Poisson's ratio for pure nickel, respectively.

Then K_{IC} and J_{IC} are plotted as a function of yield strength (σ_Y) for all

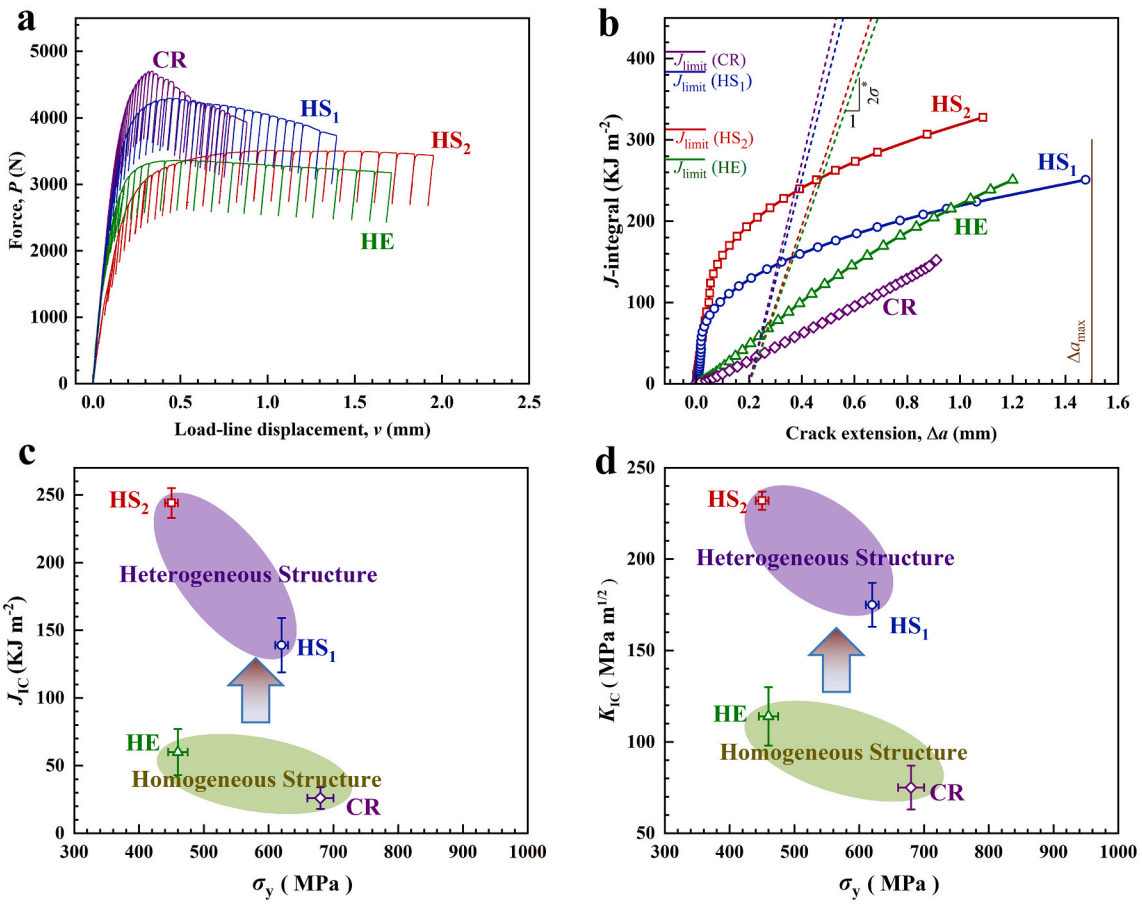

Fig. 6. The fracture toughness properties. (a) The curves of force P as a function of displacement. (b) The J-R curves. (c) K_{IC} vs. yield strength. (d) J_{IC} vs. yield strength.

four samples in Fig. 6c and d. It is observed that the heterogeneous structures (HS1, HS2 samples) show much higher fracture toughness at the similar level of yield strength, compared to the homogeneous structures (CR, HE samples). For sample, the HS2 sample with a yield strength of 450 MPa has a K_{IC} of 232 MPa $m^{1/2}$ (J_{IC}=244 kJ/m^2), which is much higher than the K_{IC} of 114 MPa $m^{1/2}$ (J_{IC}=60 kJ/m^2) for the HE sample with a nearly same yield strength of 460 MPa. As indicated from the previous research [32], the fracture toughness of the HS2 sample is even comparable to that for the CG sample of nickel (K_{IC} of 222.4 MPa $m^{1/2}$). These observations indicate that the heterogeneous structures have a much better synergy of yield strength and fracture toughness over the homogeneous structures in nickel.

3.3. Fractography and toughening mechanisms

In order to discern the toughening mechanisms of both heterogeneous and homogeneous structures, the fractographies of two samples (HS2 and HE) was examined. The SEM images for the fracture surfaces of these two samples are shown in Fig. 7. The HS2 sample displays a typical ductile fracture feature on the fracture surface although both the ductile CG areas and the "brittle-like" UFG areas exist in the HS2 sample. As indicated in Fig. 7a–c, crack initiation and propagation are fulfilled by microvoid nucleation and coalescence. High density of ductile dimples can be clearly observed on the fracture surface of the HS2 sample. The average size of the dimples is about of several tens of μm, which is consistent with the average grain size for the recrystallized CG area. It seems like that the retained UFG area also fractures with a ductile way due to the constraint by the around recrystallized CG area.

As a comparison, the fracture surface in the HE sample is macroscopically flat with occasional ridges, which result in river patterns along the crack-propagation direction (Fig. 7d–f). At crack initiation position, these polygon shapes are equal size along all direction. While, these patterns are stretched along the crack propagation direction with crack extension. With further crack extension, much larger surfaces are formed and macroscopically more flat fracture surfaces can be observed. These features indicate that the fracture process in the HE sample is cleavage-like and brittle. High density of dislocations already exist in the HE samples and the HE samples can be considered to have UFGs with substructures (dislocation tangles, dislocation walls and dislocation cells), thus the HE sample exhibits a lack of strain hardening ability, as shown in Fig. 5. Although the fracture behavior is related to the strain hardening capacity in some extent, they can't guarantee for each other [51]. For example, bulk metallic glasses (BMGs) have little strain hardening under uniaxial tension due to formation of shear bands, while BMGs have high toughness due to the microscopic plastic behaviors at a small length scale [51,52]. While, the fracture behaviors for the present HE Ni samples with UFGs (substructures, low-angle GBs) could be cleavage according to the previous paper [30,34,53]. There is a key difference between failure by void coalescence and by plastic instability (such as shear band formation) [30,51]. Previous research [30] also indicated that the real volume of the plastic zone of nanocrystalline Ni is much less than that of CG Ni due to the shear band mode for the deformation at the crack tip of nanocrystalline Ni. Thus, it is possible that shear bands are favored in the HE sample (UFGs with substructures), leading to loss of ductility and cleavage fracture. Thus, the observed much higher fracture toughness in the HS2 sample can be attributed to the ductile fracture features, as compared to the "brittle--like" fracture features in the HE sample.

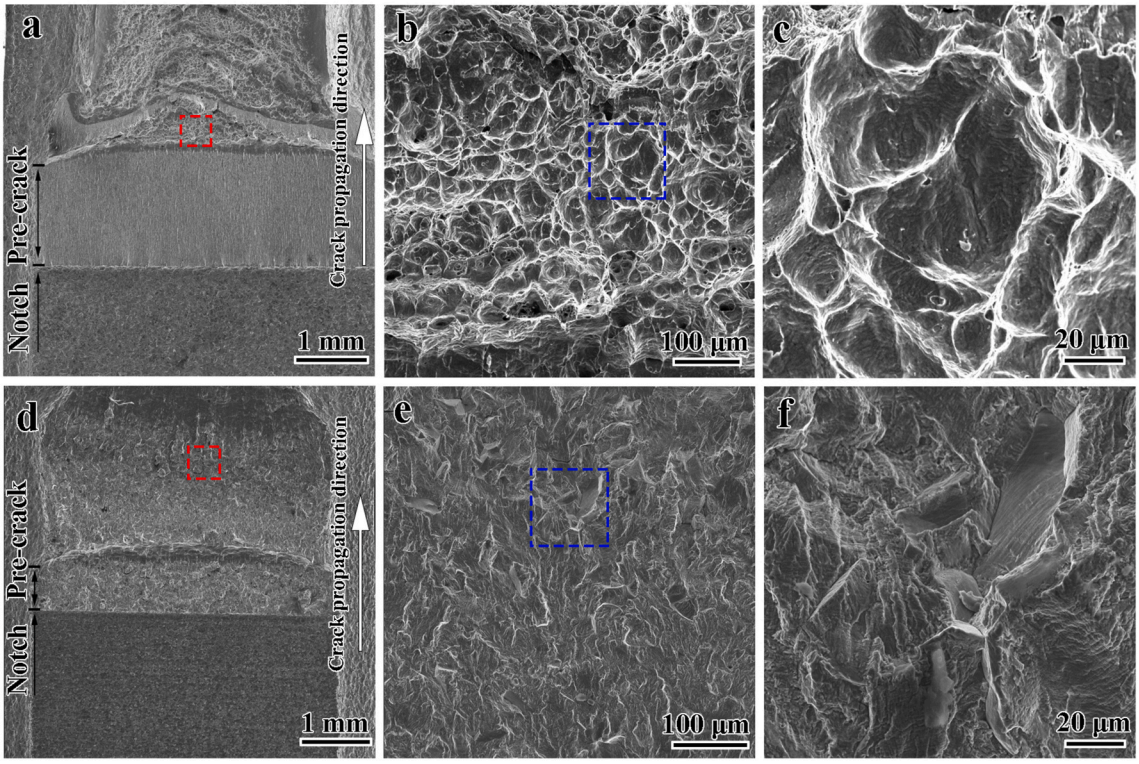

Fig. 7. The fractographies of two samples (the HS2 and HE samples). (a)–(c) The SEM images for the fracture surface of the HS2 sample. (d)–(f) The SEM images for the fracture surface of the HE sample.

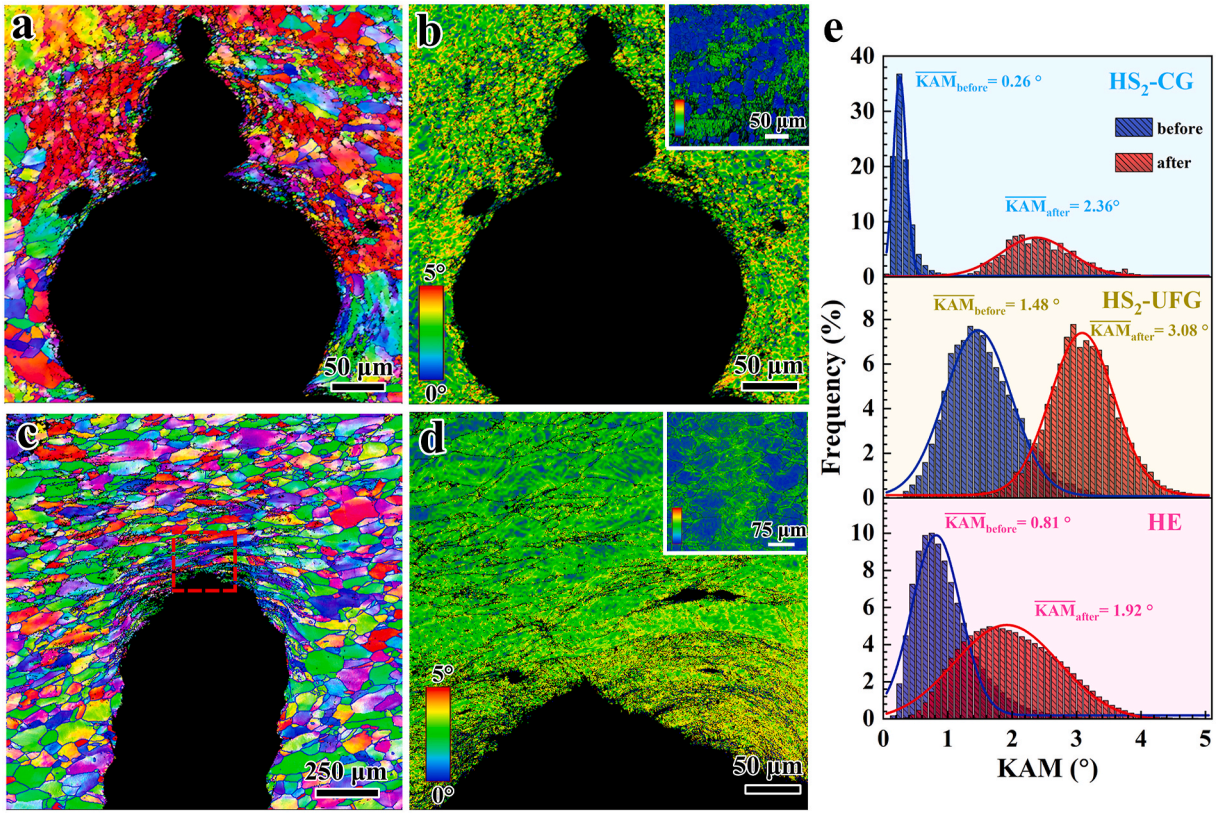

Fig. 8. (a) The EBSD IPF image of the vicinity along the propagated crack for the HS2 sample; (b) The KAM map for (a); (c) The EBSD IPF image of the vicinity along the propagated crack for the HE sample; (d) The KAM map for the marked rectangle area in (c); (e) The KAM distributions for the recrystallized CG area and the retained UFG area of the HS2 sample, and for the HE sample before and after fracture test.

To further seek the origin of the excellent synergy of strength and fracture toughness for the heterogeneous grain structures, the detailed EBSD analysis for the vicinity along the propagated crack was conducted for both the HS2 sample and the HE sample. The EBSD images were conducted on the surfaces sliced in two through the thickness to ensure the fully plane-strain deformation condition. For both samples, the EBSD scans were taken at the areas containing the crack tips. Fig. 8a shows the IPF image of the vicinity along the propagated crack for the HS2 sample. It is interesting to note that the crack path displays a gourd shape for the HS2 sample. The crack opening seems to be larger at the recrystallized CG area, while it becomes smaller at the retained UFG area. The larger crack opening at the recrystallized CG area can be attributed to the significant crack blunting induced by the dislocation behaviors and the strong strain hardening in the CGs. While, the crack opening is observed to continuously decrease toward the crack tip for the HE sample, and the grains at the vicinity of the crack tip are observed elongated severely (Fig. 8c). Thus, the higher fracture toughness in the heterogeneous structures can be partly attributed to the gourd shape for the crack path, which can result in longer crack length and dissipate more energy for better fracture toughness. The KAM maps for Fig. 8a and c are displayed in Fig. 8b and d (The corresponding insets show the KAM maps before the fracture tests). Moreover, the KAM distributions for the recrystallized CG area and the retained UFG area of the HS2 sample before and after fracture test are shown in Fig. 8e, and the KAM distributions of the HE sample (the rectangle area in Fig. 8c, right at the crack tip for the HE sample) before and after fracture test are also displayed in Fig. 8e. It is indicated that the change of the average KAM value during the fracture test is significant for the recrystallized CG area of the HS2 sample (0.26° to 2.36°), and those for the retained UFG area of the HS2 sample (1.48° to 3.08°) and the HE sample (0.81° to 1.92°) are also observed to be not small. The change of KAM value generally can be reflected to GNDs induced by plastic deformation [19]. These observations indicate that both the recrystallized CG area and the retained UFG area in the HS2 sample contribute to the strain hardening, while the recrystallized CG area has a greater impact. These observations also indicate that obvious strain hardening occurs right at the crack tip for the HE sample.

In Fig. 9, the hardening behaviors and the plastic zone information have been characterized by the micro-hardness contours around the crack tips for both the heterogeneous structures (HS1, HS2) and the homogeneous structures (CR, HE). In these figures, the plastic zone is defined as the area in which the micro-hardness should show an obvious elevation compared to that before the fracture tests. Thus, the average micro-hardness is plotted as a function of the distance from the crack tip for the four contours, and the size of the plastic zone is defined as shown in Fig. 9. The sizes of the plastic zone are found to be much larger for heterogeneous structures when compared to these for homogeneous structures. For examples, the HE sample and the HS2 sample have similar yield strength, while the size of the plastic zone for the HS2 samples (~ 2.0 mm) is much larger than that for the HE sample (~ 0.2 mm). Moreover, the size of the plastic zone for the HS1 samples is about 0.2 mm, while the CR sample shows no obvious plastic zone although the CR sample and the HS1 sample have similar yield strength. It is well known that the hardness increment during deformation can be considered as an indicator of strain hardening. Thus, the average hardness increment in the plastic zone after fracture tests is plotted as a function of the size of the plastic zone for all four samples in Fig. 9e. It is observed

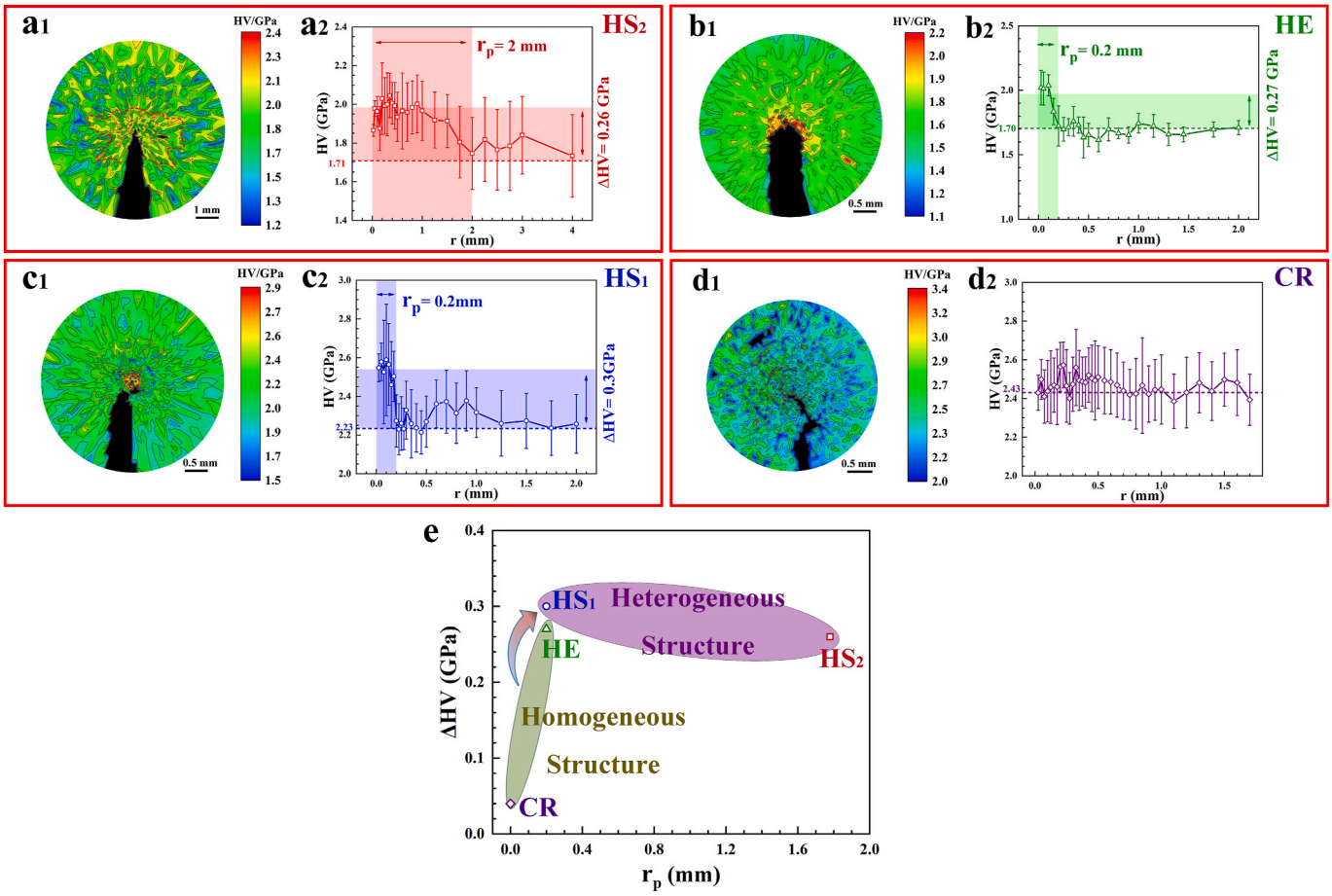

Fig. 9. The micro-hardness contours around the crack tips and the average micro-hardness as a function of the distance from the crack tip: (a1) (a2) the HS2 sample; (b1) (b2) the HE sample; (c1) (c2) the HS1 sample; (d1) (d2) the CR sample. (e) The average hardness increment in the plastic zone after fracture tests as a function of the size of the plastic zone for all four samples.

that the heterogeneous structures show a better synergy of strain hardening and plastic zone size over the homogeneous structures. Thus, the higher fracture toughness for the heterogeneous structures can be attributed to the much larger area of plastic zone around the crack tips and the much more obvious strain hardening in the plastic zone.

TEM observations have also been conducted at the crack tip areas for the HS2 sample and the HE sample to discern the origin for the strain hardening behaviors. The selected TEM bright-field images around the crack tip for the HE sample are displayed in Fig. 10. Fig. 10a and b shows the TEM images right at the crack tip, while Fig. 10c and d displays the TEM images at a position with a distance of 0.3 mm from the crack tip. As indicated in Fig. 10c and d, high density of dislocations and dislocation tangles before the fracture test are observed to be arranged into dislocation walls during the fracture process for the position with a distance of 0.3 mm from the crack tip, and this re-arrangement should not induce obvious strain hardening. While, high density of dislocations and dislocation tangles before the fracture test are observed to be evolved into dislocation cells without sharp boundaries (Fig. 10a) or UFGs with sharp GBs (Fig. 10b) right at the crack tip. The formations of dislocation cells and UFGs should provide strong strain hardening during the fracture toughness. These observations indicate that the obvious hardening area around the crack tip for the HE sample should be close to or less than 0.3 mm, which is consistent with the results for the microhardness contours in Fig. 9.

TEM bright-field images around the crack tip of the HS2 sample are shown in Fig. 11. As indicated in the TEM images of Fig. 11a and b right at the crack tip, only UFGs are found, and high density of dislocations are also observed in these UFGs. This observation indicates that the recrystallized CGs in the HS2 sample before fracture test are refined into UFGs right at the crack tip during the fracture process. This grain refinement should be the origin for the strong strain hardening at the crack tip during the fracture process for the HS2 sample. The strain hardening due to this grain refinement is very similar to the hardening in twinning-induced-plasticity (TWIP) steels by deformation twins (also called to dynamic H-P effect for TWIP steels) [54]. This effect can be called as grain-refinement-induced-plasticity (GRIP) effect, and this GRIP effect has also been observed in a CrCoNi medium entropy alloy under both quasi-static tension and dynamic shear conditions [50,55]. Both TWIP and GRIP effects can reduce the free path way for the dislocations and provide more barriers for further dislocation slip, resulting in strong strain hardening and excellent ductility/toughness. At the position with a distance of 1.2 mm from the crack tip (Fig. 11c and d), both CGs and UFGs can be found, while high density of dislocations can also be observed in the CGs, which is in sharp contrast with the clean grain interior of the CGs before the fracture test. This increased dislocation density in CGs can also induce strain hardening. At the position with a distance of 2.8 mm from the crack tip (Fig. 11e and f), the microstructure is very similar to that before the fracture test. This indicates that no obvious plastic deformation occurs at this position, which is consistent with the results from Fig. 9a.

4. Summary and concluding remarks

In the present study, heterogeneous grain structures with both recrystallized CGs and retained UFGs have been produced in pure nickel using cold rolling followed by critical annealing, and then quasi-static tensile tests and fracture tests have been conducted on both heterogeneous grain structures and homogeneous structures. The findings can be summarized as follows:

(1) The heterogeneous samples were found to have a similar yield strength and a much larger uniform elongation when compared to the homogeneous samples, which can be attributed to the stronger extra hardening by hetero-deformation for the heterogeneous structures.
(2) The heterogeneous structures were also observed to show much higher fracture toughness at the similar level of yield strength, compared to the homogeneous structures. The homogeneous HE and CR samples show the cleavage-like and brittle fracture behaviors. The superior fracture toughness in the heterogeneous structures can be attributed to the sustained ductile fracture by microvoid coalescence and dimples, which occur not only in the

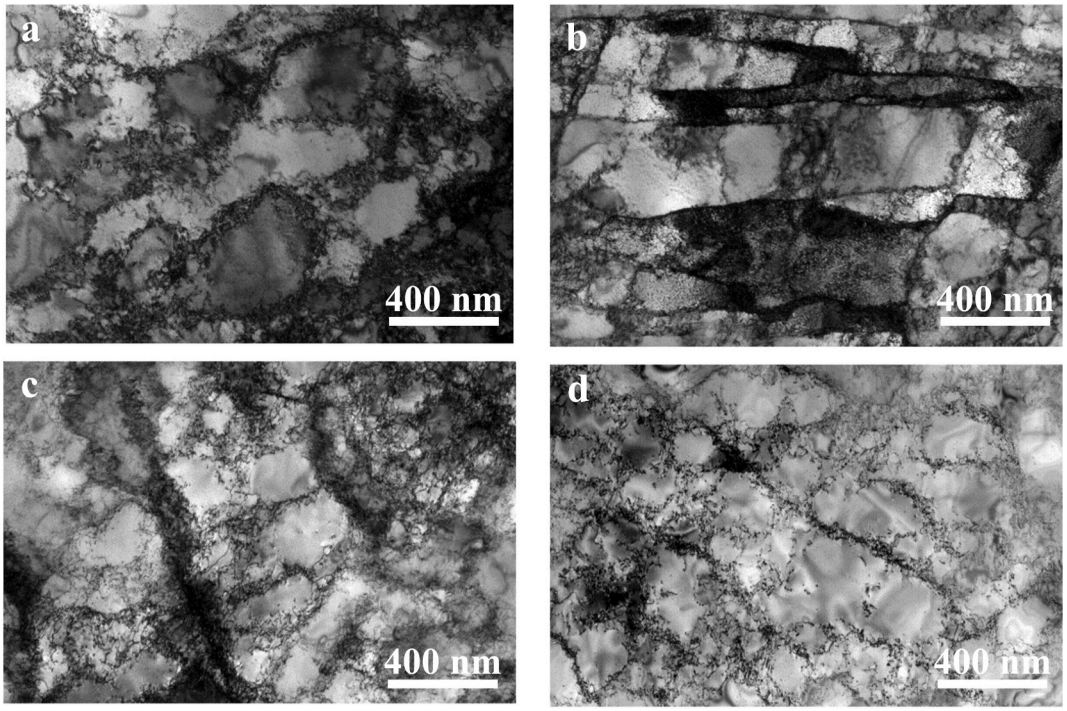

Fig. 10. The selected TEM bright-field images around the crack tip for the HE sample after fracture toughness test. (a) (b) Right at the crack tip. (c) (d) At the position with a distance of 0.3 mm from the crack tip.

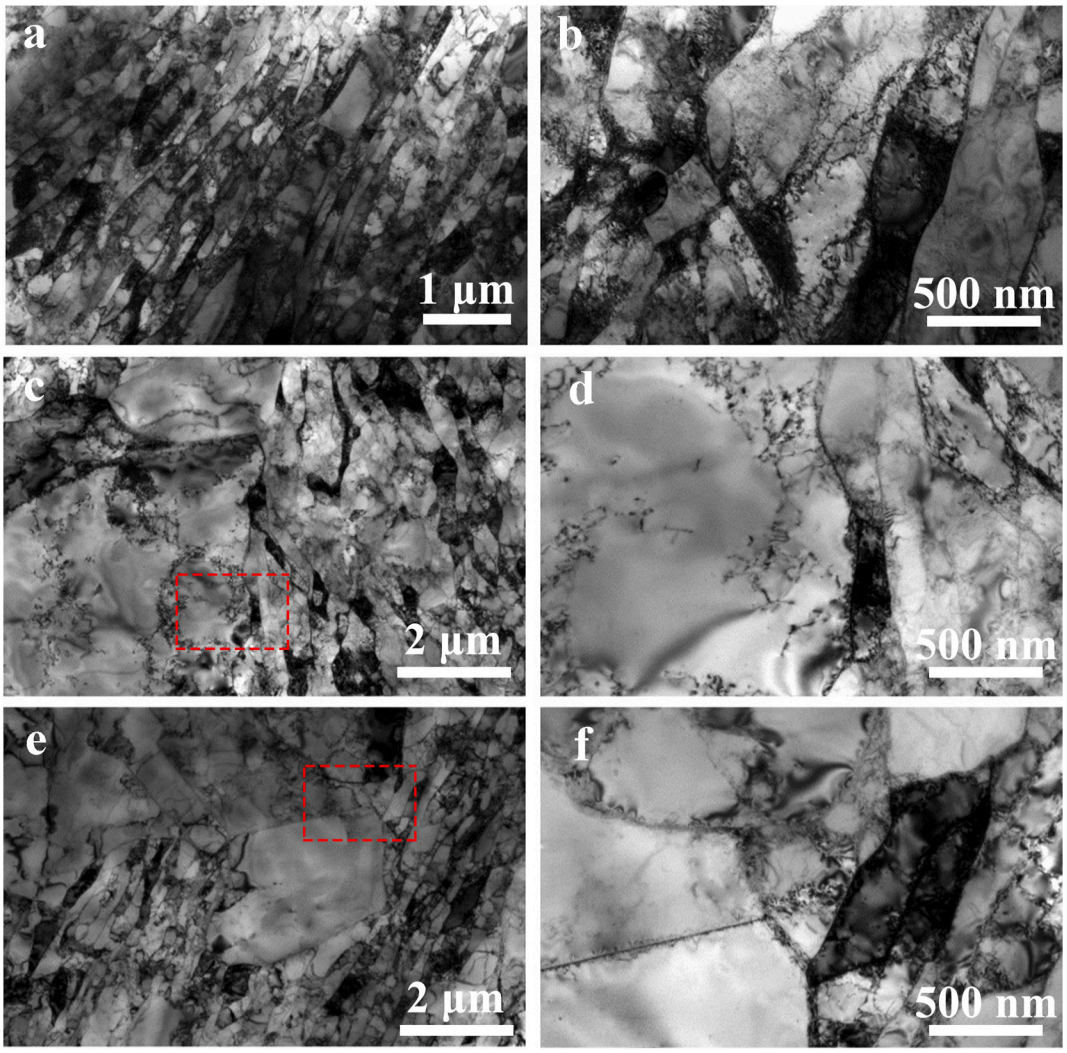

Fig. 11. The selected TEM bright-field images around the crack tip for the HS2 sample after fracture toughness test. (a) (b) Right at the crack tip. (c) (d) At the position with a distance of 1.2 mm from the crack tip. (e) (f) At the position with a distance of 2.8 mm from the crack tip.

recrystallized CG zone, but also within the retained UFG zone due to the constraint by the around recrystallized CG area.

(3) The crack path was observed to display a gourd shape for a longer crack length in the heterogeneous structures, which can dissipate more energy for better fracture toughness. According to the hardness contours around the crack tips, the heterogeneous structures show a much larger area for obvious hardening as compared to the homogeneous structures, indicating a much larger plastic zone at the crack tips for the heterogeneous structures.

(4) The CGs in the heterogeneous structures was found to be significantly refined at the crack tip, which can contribute to the strong strain hardening and the extraordinary fracture toughness. The present findings should provide insights for tailoring microstructures to achieve excellent synergy of strength and ductility/toughness in similar materials.

CRediT authorship contribution statement

Shengde Zhang: Investigation. **Muxin Yang:** Investigation. **Fuping Yuan:** Conceptualization, Writing – original draft, Supervision. **Lingling Zhou:** Investigation. **Xiaolei Wu:** Conceptualization, Supervision.

Declaration of competing interest

The authors declare that they have no known competing financial interests or personal relationships that could have appeared to influence the work reported in this paper.

Acknowledgements

This research was supported by the National Key R&D Program of China [grant number 2017YFA0204402]; the NSFC Basic Science Center Program for "Multiscale Problems in Nonlinear Mechanics" [grant number 11988102], the National Natural Science Foundation of China [grant number 52071326] and the Strategic Priority Research Program of the Chinese Academy of Sciences [grant number XDB22040503].

Appendix A. Supplementary data

Supplementary data to this article can be found online at https://doi.org/10.1016/j.msea.2021.142313.

Data availability

The raw/processed data required to reproduce these findings cannot be shared at this time due to technical or time limitations.

References

[1] R.Z. Valiev, R.K. Islamgaliev, I.V. Alexandrov, Bulk nanostructured materials from severe plastic deformation, Prog. Mater. Sci. 45 (2000) 103–189.
[2] M.A. Meyers, A. Mishra, D.J. Benson, Mechanical properties of nanocrystalline materials, Prog. Mater. Sci. 51 (2006) 427–556.
[3] K. Lu, L. Lu, S. Suresh, Strengthening materials by engineering coherent boundaries at the nanoscale, Science 324 (2009) 349–352.
[4] R.Z. Valiev, I.V. Alexandrov, Y.T. Zhu, T.C. Lowe, Paradox of strength and ductility in metals processed by severe plastic deformation, J. Mater. Res. 17 (2002) 5–8.
[5] Y.T. Zhu, X.Z. Liao, Nanostructured metals – retaining ductility, Nat. Mater. 3 (2004) 351–352.
[6] X.L. Wu, F.P. Yuan, M.X. Yang, P. Jiang, C.X. Zhang, L. Chen, Y.G. Wei, E. Ma, Nanodomained nickel unite nanocrystal strength with coarse-grain ductility, Sci. Rep. 5 (2015), 11728.
[7] K. Youssef, M. Sakaliyska, H. Bahmanpour, R. Scattergood, C. Koch, Effect of stacking fault energy on mechanical behavior of bulk nanocrystalline Cu and Cu alloys, Acta Mater. 59 (2011) 5758–5764.
[8] Y.M. Wang, E. Ma, Three strategies to achieve uniform tensile deformation in a nanostructured metal, Acta Mater. 52 (2004) 1699–1709.
[9] Y.M. Wang, M.W. Chen, F.H. Zhou, E. Ma, High tensile ductility in a nanostructured metal, Nature 419 (2002) 912–915.
[10] Y.H. Zhao, T. Topping, J.F. Bingert, J.J. Thornton, A.M. Dangelewicz, Y. Li, W. Liu, Y.T. Zhu, Y.Z. Zhou, E.L. Lavernia, High tensile ductility and strength in bulk nanostructured nickel, Adv. Mater. 20 (2008) 3028–3033.
[11] T.H. Fang, W.L. Li, N.R. Tao, K. Lu, Revealing extraordinary intrinsic tensile plasticity in gradient nano-grained copper, Science 331 (2011) 1587–1590.
[12] X.L. Wu, P. Jiang, L. Chen, F.P. Yuan, Y.T. Zhu, Extraordinary strain hardening by gradient structure, Proc. Natl. Acad. Sci. U.S.A. 111 (2014) 7197–7201.
[13] X.L. Wu, M.X. Yang, F.P. Yuan, G.L. Wu, Y.J. Wei, X.X. Huang, Y.T. Zhu, Heterogeneous lamella structure unites ultrafine grain strength with coarse-grain ductility, Proc. Natl. Acad. Sci. U.S.A. 112 (2015) 14501–14505.
[14] F.P. Yuan, D.S. Yan, J.D. Sun, L.L. Zhou, Y.T. Zhu, X.L. Wu, Ductility by shear band delocalization in the nano-layer of gradient structure, Mater. Res. Let. 7 (2019) 12–17.
[15] X.L. Wu, Y.T. Zhu, Heterogeneous materials: a new class of materials with unprecedented mechanical properties, Mater. Res. Lett. 5 (2017) 527–532.
[16] E. Ma, T. Zhu, Towards strength-ductility synergy through the design of heterogeneous nanostructures in metals, Mater. Today 20 (2017) 323–331.
[17] M.X. Yang, Y. Pan, F.P. Yuan, Y.T. Zhu, X.L. Wu, Back stress strengthening and strain hardening in gradient structure, Mater. Res. Lett. 4 (2016) 145–151.
[18] Y. Ma, M.X. Yang, F.P. Yuan, X.L. Wu, A review on heterogeneous nanostructures: a Strategy for superior mechanical properties in metals, Metals 9 (2019) 598.
[19] C.X. Huang, Y.F. Wang, X.L. Ma, S. Yin, H.W. Hoeppel, M. Goeken, X.L. Wu, H. J. Gao, Y.T. Zhu, Interface affected zone for optimal strength and ductility in heterogeneous laminate, Mater. Today 21 (2018) 713–719.
[20] P.J. Shi, W.L. Ren, T.X. Zheng, Z.M. Ren, X.L. Hou, J.C. Peng, P.F. Hu, Y.F. Gao, Y. B. Zhong, P.K. Liaw, Enhanced strength–ductility synergy in ultrafine-grained eutectic high-entropy alloys by inheriting microstructural lamellae, Nat. Commun. 10 (2019) 489.
[21] Y.T. Zhu, X.L. Wu, Perspective on hetero-deformation induced (HDI) hardening and back stress, Mater. Res. Lett. 7 (2019) 393–398.
[22] R.O. Ritchie, The conflicts between strength and toughness, Nat. Mater. 10 (2011) 817–822.
[23] E.W. Qin, L. Lu, N.R. Tao, J. Tan, K. Lu, Enhanced fracture toughness and strength in bulk nanocrystalline Cu with nanoscale twin bundles, Acta Mater. 57 (2009) 6215–6225.
[24] E.W. Qin, L. Lu, N.R. Tao, K. Lu, Enhanced fracture toughness of bulk nanocrystalline Cu with embedded nanoscale twins, Scr. Mater. 60 (2009) 539–542.
[25] L. Xiong, Z.S. You, L. Lu, Enhancing fracture toughness of nanotwinned austenitic steel by thermal annealing, Scr. Mater. 119 (2016) 55–59.
[26] L. Xiong, Z.S. You, L. Lu, Fracture behavior of an austenitic stainless steel with nanoscale deformation twins, Scr. Mater. 127 (2017) 173–177.
[27] S.S. Luo, Z.S. You, L. Lu, Intrinsic fracture toughness of bulk nanostructured Cu with nanoscale deformation twins, Scr. Mater. 133 (2017) 1–4.
[28] L. Xiong, Z.S. You, S.D. Qu, L. Lu, Fracture behavior of heterogeneous nanostructured 316L austenitic stainless steel with nanotwin bundles, Acta Mater. 150 (2018) 130–138.
[29] H.F. Li, S.G. Wang, P. Zhang, R.T. Qu, Z.F. Zhang, Crack propagation mechanisms of AISI 4340 steels with different strength and toughness, Mater. Sci. Eng. A 729 (2018) 130–140.
[30] J.J. Xie, X.L. Wu, Y.S. Hong, Shear bands at the fatigue crack tip of nanocrystalline nickel, Scr. Mater. 57 (2007) 5–8.
[31] R.A. Mirshams, C.H. Xiao, S.H. Whang, W.M. Yin, R-curve characterization of the fracture toughness of nanocrystalline nickel thin sheets, Mater. Sci. Eng. A 315 (2001) 21–27.
[32] A. Hohenwarter, R. Pippan, Fracture toughness evaluation of ultrafine-grained nickel, Scr. Mater. 64 (2011) 982–985.
[33] M.E. Launey, R.O. Ritchie, On the fracture toughness of advanced materials, Adv. Mater. 21 (2009) 2103–2110.
[34] R.Q. Cao, Q. Yu, J. Pan, Y. Lin, A. Sweet, Y. Li, R.O. Ritchie, On the exceptional damage-tolerance of gradient metallic materials, Mater. Today 32 (2020) 94–107.
[35] Y. Lin, Q. Yu, J. Pan, F.H. Duan, R.O. Ritchie, Y. Li, On the impact toughness of gradient-structured metals, Acta Mater. 193 (2020) 125–137.
[36] M.X. Yang, L.L. Zhou, C. Wang, P. Jiang, F.P. Yuan, E. Ma, X.L. Wu, High impact toughness of CrCoNi medium-entropy alloy at liquid-helium temperature, Scr. Mater. 172 (2019) 66–71.
[37] X.L. Wu, M.X. Yang, P. Jiang, C. Wang, L.L. Zhou, F.P. Yuan, E. Ma, Deformation nanotwins suppress shear banding during impact test of CrCoNi medium-entropy alloy, Scr. Mater. 178 (2020) 452–456.
[38] R. Pippan, A. Hohenwarter, The importance of fracture toughness in ultrafine and nanocrystalline bulk materials, Mater. Res. Lett. 4 (2016) 127–136.
[39] P. Cavaliere, Crack tip plasticity in plastically graded Ni-W electrodeposited nanocrystalline alloys, Comput. Mater. Sci. 41 (2008) 440–449.
[40] B. Gludovatz, A. Hohenwarter, D. Catoor, E.H. Chang, E.P. George, R.O. Ritchie, A fracture-resistant high-entropy alloy for cryogenic applications, Science 345 (2014) 1153–1158.
[41] B. Gludovatz, A. Hohenwarter, K.V. Thurston, H. Bei, Z. Wu, E.P. George, R. O. Ritchie, Exceptional damage-tolerance of a medium-entropy alloy CrCoNi at cryogenic temperatures, Nat. Commun. 7 (2016), 10602.
[42] M. Furukawa, Y. Iwahashi, Z. Horita, M. Nemoto, T.G. Langdon, The shearing characteristics associated with equal-channel angular pressing, Mater. Sci. Eng. A 257 (1998) 328–332.
[43] M. Shepelenko, L. Klinger, E. Rabkin, A. Berner, D. Prokoshkina, G. Reglitz, J. Fiebig, G. Wilde, S.V. Divinski, Recovery, recrystallization and diffusion in cold-rolled Ni, Int. J. Mater. Res. 106 (2015) 1–11.
[44] P.W. Trimby, Y. Cao, Z. Chen, S. Han, K.J. Hemker, J. Lian, X. Liao, P. Rottmann, S. Samudrala, J. Sun, J.T. Wang, J. Wheeler, J.M. Cairney, Characterizing deformed ultrafine-grained and nanocrystalline materials using transmission Kikuchi diffraction in a scanning electron microscope, Acta Mater. 62 (2014) 69–80.
[45] P.P. Bhattacharjee, R.K. Ray, A. Upadhyaya, Development of cube texture in pure Ni, Ni-W and Ni-Mo alloys prepared by the powder metallurgy route, Scr. Mater. 53 (2005) 1477–1481.
[46] A.L. Etter, M.H. Mathon, T. Baudin, V. Branger, R. Penelle, Influence of the cold rolled reduction on the stored energy and the recrystallization texture in a Fe-53% Ni alloy, Scr. Mater. 46 (2002) 311–317.
[47] S. Basu, E. Dogan, B. Kondori, I. Karaman, A.A. Benzerga, Towards designing anisotropy for ductility enhancement: a theory-driven investigation in Mg-alloys, Acta Mater. 131 (2017) 349–362.
[48] A. Hohenwarter, R. Pippan, Fracture of ECAP-deformed iron and the role of extrinsic toughening mechanisms, Acta Mater. 61 (2013) 2973–2983.
[49] M.N. Hasan, Y.F. Liu, X.H. An, J. Gu, M. Song, Y. Cao, Y.S. Li, Y.T. Zhu, X.Z. Liao, Simultaneously enhancing strength and ductility of a high-entropy alloy via gradient hierarchical microstructures, Int. J. Plast. 123 (2019) 178–195.
[50] M.X. Yang, D.S. Yan, F.P. Yuan, P. Jiang, E. Ma, X.L. Wu, Dynamically reinforced heterogeneous grain structure prolongs ductility in a medium-entropy alloy with gigapascal yield strength, Proc. Natl. Acad. Sci. U.S.A. 115 (2018) 7224–7229.
[51] A. Pineau, A.A. Benzerga, T. Pardoen, Failure of metals I – brittle and ductile fracture, Acta Mater. 107 (2016) 424–483.
[52] J. Xu, U. Ramamurty, E. Ma, The fracture toughness of bulk metallic glasses, J. Occup. Med. 62 (2010) 10–18.
[53] R.A. Mirshams, C.H. Xiao, S.H. Whang, W.M. Yin, R-Curve characterization of the fracture toughness of nanocrystalline nickel thin sheets, Mater. Sci. Eng. A 315 (2001) 21–27.
[54] O. Bouaziz, Strain-Hardening of twinning-induced plasticity steels, Scr. Mater. 66 (2012) 982–985.
[55] Y. Ma, F.P. Yuan, M.X. Yang, P. Jiang, E. Ma, X.L. Wu, Dynamic shear deformation of a CrCoNi medium-entropy alloy with heterogeneous grain structures, Acta Mater. 148 (2018) 407–418.